

# Valorization of cellulose-doped lignin: application of cellulose-doped lignin-derived activated carbon in capacitors and investigation of its textural properties and electrochemical performance

Liangcai Wang (✉ [694452344@qq.com](mailto:694452344@qq.com))

Nanjing Forestry University

Xin Feng

Nanjing Forestry University

Huanhuan Ma

Nanjing Forestry University

Jielong Wu

Nanjing Forestry University

Yu Chen

Nanjing Forestry University

Jianbin Zhou

Nanjing Forestry University

---

## Research Article

**Keywords:** cellulose-doped apricot shell lignin, activated carbon, textural properties, specific capacitance, capacitors

**Posted Date:** March 29th, 2021

**DOI:** <https://doi.org/10.21203/rs.3.rs-279922/v1>

**License:**   This work is licensed under a Creative Commons Attribution 4.0 International License.

[Read Full License](#)

---

# Abstract

This work provides an idea for efficient and harmless utilization of lignin and further evaluated the textural properties of lignin-derived activated carbon/specific capacitance relationship. The yield of cellulose-doped apricot shell lignin (ASLC) was 30.42%.  $\text{H}_3\text{PO}_4/\text{KOH}$  was used to assist the preparation of ASLC-derived activated carbon (AAC) for capacitors. The specific surface areas of the as-obtained AAC-P-3 and AAC-K-2 were  $1475.16 \text{ m}^2/\text{g}$  and  $2136.56 \text{ m}^2/\text{g}$ , respectively. The specific capacitances of AAC-P-3 and AAC-K-2 were  $169.14 \text{ F/g}$  and  $236.00 \text{ F/g}$ , respectively, upon the current density of  $0.50 \text{ A/g}$ . In capacitors containing aqueous KOH as the electrolyte, the  $\text{AR}^2$  (0.983) between specific surface area and specific capacitance was highest, followed by the  $\text{AR}^2$  (0.978) between  $V_{\text{micro}}/V_{\text{meso}}$  and specific capacitance, the  $\text{AR}^2$  (0.975) between pore-wall thickness and specific capacitance. Consequently, the specific capacitances of the AACs depend not only the specific surface area, but also on the  $V_{\text{micro}}/V_{\text{meso}}$ , pore-wall thickness, and  $V_{\text{micro}}$ .

## 1. Introduction

With the consumption of fossil fuels, environmental pollution and potential energy crisis are gradually increasing. Therefore, the urgent demand for renewable energy is attracting more and more attention. However, most renewable energies have unstable characteristics. These have spurred a great deal of investigation on stable energy storage devices.<sup>1</sup> Among many energy storage devices, supercapacitors are overwhelmingly attractive, resulting from their many advantages (e.g. fast charge/discharge rate, high power density, excellent cycle stability).<sup>2-4</sup> For supercapacitors, the role of electrode materials is exceedingly critical. Among many electrode materials, porous carbon has a host of advantages, including but not limited to the high specific surface area, porous structure, and excellent chemical stability.<sup>5</sup>

As we all know, as a kind of porous carbon, biomass-derived activated carbon has distinct advantages as an electrode material, resulting from its large specific surface, stability, as well as benign raw materials.<sup>6-9</sup> Examples include camellia petals, cornstalk, popcorn, and bamboo are employed as feedstock for the preparation of biomass-derived activated carbon for energy storage.<sup>10-14</sup> Compared with the mentioned biomass, lignin has highly competitive advantages because it possesses a 3D network structure, higher density, and abundant resources.<sup>15,16</sup> Consequently, we can infer that lignin-derived activated carbon has promising application in supercapacitor electrodes. Unfortunately, most of the lignin in the papermaking process is wasted and causes water pollution. To address the above problems, the investigation on the efficient and harmless utilization of lignin has almost focused on lignin-based adhesives and the pyrolysis mechanism of lignin model compounds.<sup>17-19</sup> However, the preparation and modification processes of lignin-based adhesives are complicated and accompanied by high costs. Thus, it is hard to achieve industrialization. Meanwhile, due to the technique limitation, the lignin produced in the papermaking process has a minor amount of cellulose, which results in it different from the lignin model compounds.

Moreover, to obtain high-performance supercapacitors, a multitude of strategies for increasing the specific surface area of porous carbon have been reported.<sup>20-22</sup> For example, Shang et al.<sup>23</sup> prepared walnut shell-derived activated carbon with a specific surface area of 3577 m<sup>2</sup>/g via carbonization and activation and employed it in capacitors. The results showed that it has excellent specific capacitance. Díez et al.<sup>24</sup> synthesized tannic acid-derived porous carbon with a high specific surface area (2750 m<sup>2</sup>/g) by a salt template-assisted chemical activation approach. This tannic acid-derived porous carbon exhibited a superior specific capacitance as high as 260 F/g. Luo et al.<sup>25</sup> used crayfish shells and bio-oil as raw materials to synthesis porous carbon with a specific surface area of 3095 m<sup>2</sup>/g. This porous carbon exhibited an excellent specific capacitance. These previous studies achieved remarkable advances in enhancing the porous carbon-specific surface area and the performance of supercapacitors. In addition, these novel works imply that the specific surface area seems to be positively linearly related to specific capacitance. Nonetheless, there have been no investigations into a systematic study of the relationship between the textural properties of porous carbon and specific capacitance in the literature. Consequently, the objectives of this work to give a route for the valorization of cellulose-doped lignin, and further investigate the textural properties/ specific capacitance relationship.

ASLC and apricot shell cellulose were extracted, and the two were compared. Besides, the reasons for choosing ASLC to synthesize AAC were given. To improve the reliability of the conclusion, two activation methods (H<sub>3</sub>PO<sub>4</sub> and KOH) were employed in the case study of ASLC. As a novel and crucial textural property, the pore-wall thickness was calculated in this work. Besides, the specific capacitance was employed to correlate with the textural properties. The activated carbon prepared by H<sub>3</sub>PO<sub>4</sub> activation was rich in mesopores, while the activated carbon prepared by KOH activation was almost all micropores, with fewer mesopores. When the current density was 0.5 A/g, the specific capacitance of AAC-K-2 (S<sub>BET</sub>=2136.56 m<sup>2</sup>/g) was 236.00 F/g. On the other hand, the specific capacitances of the AACs depend not only the specific surface area, but also on the V<sub>micro</sub>/V<sub>meso</sub>, pore-wall thickness, and V<sub>micro</sub>.

## 2. Experimental Section

### 2.1 Materials

Apricot shell was obtained from the Pingquan, Heibei Province of China. Before the experiment, the apricot shell was ground into powder. Subsequently, dried at 105°C for 24 h. The extractions of apricot shell cellulose and apricot shell lignin were described in our previous work.<sup>26</sup> For proximate and ultimate analysis, a detailed introduction has been recorded in our previous study.<sup>26</sup> The results are exhibited in Table 1.

### 2.2 Methods

#### 2.2.1 FTIR and thermogravimetric analysis

For apricot shell cellulose and ASLC, the infrared spectroscopy study was performed using a VERTEX 80V Fourier infrared spectrometer (Bruker, Karlsruhe, Germany). Thermogravimetric analysis was monitored employing a thermogravimetric analyzer (Q500, TA Instruments, USA) with a heating rate of 10°C/min from room temperature to 800 °C under a flow of nitrogen.

### 2.2.2 AAC synthesis

AAC was obtained via mixing ASLC with H<sub>3</sub>PO<sub>4</sub>/KOH and then employing established procedures for activation. In detail, a mixture of ASLC and H<sub>3</sub>PO<sub>4</sub>/KOH in a nickel boat was heated to 550 °C (at a heating rate of 10 °C/min) upon a flow of N<sub>2</sub> in a tube furnace, and then the temperature was maintained for 1 h. The tube furnace was cooled, the black samples were taken out, washed with distilled water, and dried in an oven at 105°C for 6 h to remove moisture.

### 2.2.3 Sample labels

The AACs were denoted as AAC-P-X, AAC-K-Y, respectively, where P represents P<sub>3</sub>PO<sub>4</sub> (mass fraction was 60%); K is KOH; X and Y represent the ratio of the weight of H<sub>3</sub>PO<sub>4</sub> solution to the weight of ASLC, the ratio of the weight of KOH to the weight of ASLC, respectively. For example, AAC-K-1 manifests the activated carbon from ASLC at the ratio of the weight of KOH to the weight of ASLC was 1.

### 2.2.4 Characterization

Nitrogen adsorption/desorption isotherms were recorded using an automatic analyzer (Q10, Quantachrome Corporation, Boynton Beach, USA). The BET equation was applied for specific surface area calculation, while the pore size was obtained by a Non-local Density Functional Theory (NLDFT). The morphology and structure of the samples were observed by scanning electron microscopy (SEM, JSM-7600F, JOL Ltd., Tokyo, Japan).

### 2.2.5 Electrode preparation

The working electrodes were composed of carbon black, polytetrafluoroethylene, and AAC with a weight ratio of 1:1:8. The mixture was stirred with alcohol to form a slurry and coated on nickel foams (100 mm<sup>2</sup>). Subsequently, dried under vacuum at 60°C for 10 h, after which, pressed at a pressure of 10 MPa to make the electrodes.

### 2.2.6 Electrochemical tests

Electrochemical measurements were carried out in a conventional three-electrode system with a 6 mol/L KOH aqueous solution as the electrolyte. The Hg/HgO electrode and the platinum electrode were employed as reference electrodes and counter electrodes, respectively. Cyclic voltammetry (CV), galvanostatic charge-discharge (GCD), and electrochemical impedance spectroscopy (EIS) were determined by an electrochemical workstation (CHI 660E, Shanghai Chenhua, China). The specific capacitance was calculated according to the following formula:

$$C = \frac{I \times \Delta t}{\Delta V \times m}$$

where, C, I, and  $\Delta t$  represent the specific capacitance (F/g), the discharge current (A), and the discharge time (s), respectively.  $\Delta V$  is the potential window (V); m represents the weight of the AAC on the working electrode (g).

## 3. Results And Discussion

### 3.1 FTIR spectra of apricot shell cellulose and ASLC

The yield of ASLC higher than that of apricot shell cellulose, as listed in Table 1. In reviewing the literature, the characteristic absorption peaks of cellulose  $\beta$ -glycosidic bond at  $\sim 895 \text{ cm}^{-1}$ ,  $\sim 1056 \text{ cm}^{-1}$ , and  $\sim 1162 \text{ cm}^{-1}$ .<sup>27</sup> The characteristic absorption peaks of benzene ring skeleton of lignin at  $\sim 1430 \text{ cm}^{-1}$ ,  $\sim 1508 \text{ cm}^{-1}$ , and  $\sim 1615 \text{ cm}^{-1}$ .<sup>28, 29</sup> Fig. 1 (a) indicates that there are absorption peaks at wavenumbers of  $895 \text{ cm}^{-1}$ ,  $1056 \text{ cm}^{-1}$ , and  $1162 \text{ cm}^{-1}$ , suggesting the presence of cellulose  $\beta$ -glycosidic bond in apricot shell cellulose. The stretching vibration of the  $-\text{CH}_3/-\text{CH}_2$  at  $\sim 1461 \text{ cm}^{-1}$ . The absorption peaks of syringyl at  $\sim 1322 \text{ cm}^{-1}$  and  $\sim 1112 \text{ cm}^{-1}$ . Additionally, the absorption peak at wavenumber  $1270 \text{ cm}^{-1}$  or  $1215 \text{ cm}^{-1}$  indicates the presence of guaiacol.<sup>28, 29</sup> As a result,  $-\text{CH}_3/-\text{CH}_2$ , benzene ring skeleton, syringyl, and guaiacol were existed in apricot shell lignin, as shown in Fig. 1 (b). Notably, Fig. 1 (b) equally indicates that apricot shell lignin has a minor amount of cellulose (apricot shell lignin was doped with cellulose), which was due to the limitation of the experiment. Thus, apricot shell lignin was doped with cellulose was denoted as ASLC.

### 3.2 Thermogravimetric analysis

To further investigate the pyrolysis characteristics of apricot shell cellulose and ASLC, the weight loss (TG) and the rate of weight loss (DTG) upon the heating rate of  $10 \text{ }^\circ\text{C}/\text{min}$  were analyzed, as exhibited in Fig. 2. Fig. 2 (a) shows that the pyrolysis processes of the apricot shell, apricot shell cellulose, and ASLC were composed of dry dehydration stage, pyrolysis stage, and pyrolysis-carbonization stages. The first stage was a slow weight loss stage, while the second and third stages were rapid devolatilization stages. In dry dehydration stage, apricot shell cellulose possesses the largest weight loss, followed by apricot shell and ASLC. In the two hind stages, apricot shell, apricot shell cellulose, and ASLC lose a lot of weight and formed significant weight-loss peaks. Different from the apricot shell and ASLC, apricot shell cellulose contains only one significant weight-loss peak. Similar results were also found for cellulose model components.<sup>30</sup> Besides, the two significant weight-loss peaks formed during the pyrolysis of ASLC were similar to that of the lignin model components.<sup>30, 31</sup> Notably, for the apricot shell, apricot shell cellulose, and ASLC, the pyrolysis-carbonization processes were completed at  $\sim 550 \text{ }^\circ\text{C}$ . Consequently, in preparation for activated carbon, considering the property and cost, the activation

temperature was 550 °C. Furthermore, the pyrolysis residues of the apricot shell, apricot shell cellulose, and ASLC were 24.49 mass%, 16.96 mass%, and 33.13 mass%, respectively. Compared with the yield of the apricot shell and apricot shell cellulose pyrolysis residues, the yield of ASLC pyrolysis residue was higher. Accordingly, in the following experiments, the ASLC was selected if not mentioned as otherwise.

### 3.3 Characterization of AAC

#### 3.3.1 Textural properties of AAC

H<sub>3</sub>PO<sub>4</sub> and KOH are generally used as activators for the preparation of activated carbon.<sup>32, 33</sup> As we all know, N<sub>2</sub> adsorption and desorption isotherms at low relative pressure indicate micropores are filled; in other words, there are a host of micropores. At moderate relative pressure, isotherms with a hysteresis loop demonstrate the presence of mesopores. The steep rise of isotherms at high relative pressure exhibits capillary condensation in the macropores; that is to say that the existence of macropores. Fig. 3 indicates that the AAC has hierarchical structures of porosity. At low relative pressure, the N<sub>2</sub> adsorption/desorption isotherm of AAC-K-2 is the steepest, followed by AAC-K-1, AAC-P-3, and AAC-P-4. Consequently, the order of the micropore specific pore volume ( $V_{\text{micro}}$ ) of AAC was determined: AAC-K-2 > AAC-K-1 > AAC-P-3 > AAC-P-4. Inversely, the N<sub>2</sub> adsorption/desorption isotherm of AAC-K-2 was the gentlest upon moderate relative pressure, followed by AAC-K-1, AAC-P-3, and AAC-P-4, which means AAC-K-2 has the lowest mesopore specific pore volume ( $V_{\text{meso}}$ ) and AAC-P-4 has the highest  $V_{\text{meso}}$ . On the other hand, the N<sub>2</sub> adsorption and desorption isotherms of AAC-K-2, AAC-K-1, AAC-P-3, and AAC-P-4 display different degrees of an upward trend at high relative pressure, which indicates that AAC-K-2, AAC-K-1, AAC-P-3, and AAC-P-4 have macroporous structures. These results indicated the hierarchical micro/meso/macroporous nature of AAC. Moreover, the textural properties of AAC can be obtained by analyzing the adsorption and desorption isotherms of N<sub>2</sub>, as shown in Table 2.

Compared to AAC-K-2 (2136.56 m<sup>2</sup>/g), the specific surface areas of AAC-K-1, AAC-P-3, AAC-P-4 decreased to 1669.94 m<sup>2</sup>/g, 1475.16 m<sup>2</sup>/g, and 1370.35 m<sup>2</sup>/g, respectively. Montane et al.<sup>32</sup> used H<sub>3</sub>PO<sub>4</sub> as an activator to synthesize lignin-based activated carbon with a specific surface area of ~1000 m<sup>2</sup>/g. Zhang et al.<sup>34</sup> indicated the specific surface area of KOH-assisted synthesis of activated carbon was 1672 m<sup>2</sup>/g. In other words, the specific surface area of lignin-based activated carbon lower than that of AAC-P-3 and AAC-P-4, and the specific surface area of KOH-assisted synthesis of activated carbon lower than that of AAC-K-2. Moreover, the  $V_{\text{micro}}/V_{\text{meso}}$  values of AACs were over 45.00%, especially AAC-K-2, its  $V_{\text{micro}}/V_{\text{meso}}$  value was as high as 375.27%, these results indicate that AACs with well-developed micropores. Compared with the AAC-P-3 and AAC-P-4, the average pore sizes of AAC-K-1 and AAC-K-2 were narrower. These results were consistent with the conclusion that the micropore specific pore volumes of AAC-K-1 and AAC-K-2 were higher. In this work, the pore-wall thickness was calculated by the following formula: Pore-wall thickness =  $2/(\rho S_{\text{BET}})$ , where  $\rho = 2.2 \text{ g/cm}^3$  represents the density of carbon

wall equated to the density of graphite.<sup>35, 36</sup> The order of the pore-wall thickness of AAC was established: AAC-P-4 > AAC-P-3 > AAC-K-1 > AAC-K-2, as listed in Table 2.

To further understand the pore structures of AAC, the pore size distribution is presented in Fig. 4. Unlike AAC-P-3 and AAC-P-4, AAC-K-1 and AAC-K-2 have intensely abundant micropores, especially micropores with a pore size of  $\sim 0.75$  nm. Furthermore, the micropores of AAC-P-3 and AAC-P-4 were primarily concentrated in the range of 1-2 nm, and the micropores below 1 nm were few. For mesopores within the range of 2-5 nm, AAC-K-1 and AAC-K-2 have only a minor amount of distribution, while AAC-P-3 and AAC-P-4 possess a majority of distribution. Interestingly, the previous study has shown that porous materials rich in 2-5 nm are more beneficial to the adsorption of dioxin;<sup>37</sup> from this, we can infer that AAC equally possesses a promising application in removing dioxins. On the other hand, the activated carbon prepared by  $H_3PO_4$  activation was rich in mesopores, while the activated carbon prepared by KOH activation was almost all micropores, with fewer mesopores. Consequently, in actual production, different activation strategies can be selected according to activated carbon requirements. According to literature, porous materials possess high specific surface area and proper pore size distribution hold a promising application as electrode materials for capacitors.<sup>38, 39</sup> Sudhan et al.<sup>40</sup> prepared a rice straw-derived activated carbon that possesses a specific surface area of  $1007 \text{ m}^2/\text{g}$  and employed it as an electrode material for supercapacitors. Notably, the specific surface areas of AAC-P-3, AAC-P-4, AAC-K-1, and AAC-K-2 are higher than  $1007 \text{ m}^2/\text{g}$ , especially AAC-K-1 and AAC-K-2. As a result, AAC-P-3, AAC-P-4, AAC-K-1, and AAC-K-2 also have a certain value in the application of electrode materials for capacitors.

### 3.3.2 Micro-morphology of AAC

To observe the natural hierarchical porous structure of AAC more intuitively, SEM tests using AAC-P-3 and AAC-K-2 as examples were performed. Fig. 5(a) indicates that the surface of the AAC-P-3 is similar to the honeycomb, which means AAC-P-3 has an enriched pore structure. It is worth noting that the 3D architecture with hierarchical structures is presented in Fig. 5(b). Moreover, Fig. 5 (b) shows that the porosity is composed of irregularly oriented narrow pores. These micro-morphologies are consistent with and also more intuitively than the results of  $N_2$  adsorption and desorption isotherms.

### 3.4 Electrochemical performance of AAC

Fig. 6 (a) demonstrates GCD curves of AAC-P-3, AAC-P-4, AAC-K-1, and AAC-K-2 at the current density was  $0.5 \text{ A/g}$ . As we all know, if the GCD curve is approximately an isosceles triangle, it indicates an ideal double-layer capacitor behavior.<sup>41</sup> AAC-P-3, AAC-P-4, AAC-K-1, and AAC-K-2 have excellent double-layer capacitor behavior. The specific capacitances of AAC-P-3, AAC-P-4, AAC-K-1, and AAC-K-2 were  $169.14 \text{ F/g}$ ,  $159.98 \text{ F/g}$ ,  $188.50 \text{ F/g}$ , and  $236.00 \text{ F/g}$ , respectively. Consequently, considering the specific capacitance and different preparation processes, AAC-P-3 and AAC-K-2 were choose for the CV test.

The capacitance behavior shown in these CV curves has belike quasi-rectangular shapes accompany by some humps, resulting from the combined effects of electrical double-layer capacitance and

pseudocapacitance.<sup>42, 43</sup> The CV curves of AAC-P-3 and AAC-K-2 upon various scan rates are shown in Fig. 6 (b) and (c), respectively. CV curve is similar to a rectangle, which means the electrolyte can diffuse into the micropores within a sufficient time. In other words, the charge and discharge reversibility are better. Fig. 6 (b) and (c) indicate the AAC-P-3 and AAC-K-2 possess a better charge/discharge reversibility at a low scan rate (5-20 mv/s). Additionally, the resistance of micropores is higher than that of mesopores and macropores. Which results in the electrolyte ions cannot quickly enter the micropores upon a high scan rate. Hence, with an increase in scan rate (>20 mv/s), the degree of CV curve deviation from the rectangle gradually increased. Nonetheless, none of them exhibited redox peaks, demonstrating that the AAC-P-3 and AAC-K-2 have excellent electrochemical stability.

On the other hand, the specific capacitances of AAC-P-3, AAC-P-4, AAC-K-1, and AAC-K-2 are listed in Table 3. Meanwhile, the plot of specific capacitance variation of AAC is given in Fig. 7. In brief, the specific capacitances of AAC-P-3 and AAC-P-4 were comparable to that of the reported commercially available specific capacitances of supercapacitors. However, the specific capacitances of AAC-K-1 and AAC-K-2 were over the specific capacitances of commercially available supercapacitors.<sup>44</sup> With an increase in the current density, the specific capacitances of AAC-P-3, AAC-P-4, AAC-K-1, and AAC-K-2 gradually decreased, which were similar to the results of previous studies.<sup>45-49</sup> The order of the specific capacitances of AAC-P-3, AAC-P-4, AAC-K-1, and AAC-K-2 was established at the same current density: AAC-K-2 > AAC-K-1 > AAC-P-3 > AAC-P-4. Notably, at the current density was 0.50 A/g, the specific capacitance of AAC-P-3 was higher than that of rice straw-derived activated carbon and jute stick-derived activated carbon.<sup>40, 50</sup> Moreover, the capacitance retention rates of AACs at 10.00 A/g exceed 67.39%.

EIS was employed to further understand the electrochemical performances of AAC-P-3, AAC-P-4, AAC-K-1, and AAC-K-2, as shown in Fig. 6 (d). As we all know, the low-frequency region and high-frequency region indicate the charge diffusion-limited process and the resistance of charge transfer at the interface between the electrolyte and active materials, respectively.<sup>51, 52</sup> Compared with the Rct values of AAC-P-3, AAC-P-4, and AAC-K-1 (~ 1.9  $\Omega$ ), the Rct value of AAC-K-2 was higher (~ 2.25 $\Omega$ ). In addition, the high slope in the low-frequency region shows that AAC-P-3, AAC-P-4, AAC-K-1, and AAC-K-2 have pleasurable capacitance performance.

### 3.5 Textural properties/specific capacitance relationship

For porous materials, the textural property directly affects the performance of porous materials.<sup>53, 54</sup> For instance, micropores provide a large surface area for ion adsorption, mesopores serve as transport channels into the micropores, and macropores serve as ion-buffering reservoirs, which can reduce the diffusion distance of ions.<sup>55</sup> Furthermore, some studies have exhibited the specific surface area affects specific capacitance.<sup>56-58</sup> It is worth noting that the specific surface area is only one of the textural properties. As a result, it is necessary to systematically understand the influence of textural properties (e.g. specific surface area, specific pore volume, pore-wall thickness) on specific capacitance.

In this work, linear fitting was used to evaluate the relationship between textural properties and specific capacitance. Thus, the data in Table 2 was associated with the data in Table 3, as shown in Fig. 8. The average values of the correlation coefficients ( $AR^2$ ) in Fig. 8 (a), (b), (c), (d), (e), (f), (g) were calculated respectively, which were 0.983, 0.312, 0.956, 0.808, 0.978, 0.837, 0.975. Among these, the  $AR^2$  (0.983) between specific surface area and specific capacitance was highest, followed by the  $AR^2$  (0.978) between  $V_{\text{micro}}/V_{\text{meso}}$  and specific capacitance, the  $AR^2$  (0.975) between pore-wall thickness and specific capacitance; from this, we can infer that the specific surface area plays a key role in specific capacitance. A similar phenomenon has been observed in previous studies.<sup>56-58</sup> It is worth noting that 0.983, 0.978, 0.975, 0.956 are very close and are all higher than 0.95. Consequently, the specific capacitances of the AACs depend not only the specific surface area, but also on the  $V_{\text{micro}}/V_{\text{meso}}$ , pore-wall thickness, and  $V_{\text{micro}}$ . On the other hand, the  $AR^2$  (0.312) between  $V_t$  and specific capacitance was the lowest; that is to say that  $V_t$  and the specific capacitance were not linearly positively correlated. Based on the  $AR^2$ , we can infer that the specific surface area,  $V_{\text{micro}}/V_{\text{meso}}$ , pore-wall thickness, and  $V_{\text{micro}}$  can be used as a universal predictor of specific capacitance upon employed KOH solution as the electrolyte.

## 4. Conclusions

The approach of preparing AACs for capacitors by  $H_3PO_4$ /KOH activation was feasible, and their specific capacitance was slightly higher than the specific capacitances of commercially available supercapacitors. The AACs prepared by  $H_3PO_4$  activation were rich in mesopores, while the AACs prepared by KOH activation were almost all micropores, with fewer mesopores. We have shown that the specific capacitance of AAC-K-2 (2136.56  $m^2/g$ ) upon a current density of 0.5 A/g was 236.00 F/g. On the other hand, the specific surface area,  $V_{\text{micro}}/V_{\text{meso}}$ , and pore-wall thickness of AACs were linearly related to their specific capacitance. As a result, in the case of KOH solution as the electrolyte, the specific surface area,  $V_{\text{micro}}/V_{\text{meso}}$ , pore-wall thickness, and  $V_{\text{micro}}$  can be used as a universal predictor of specific capacitance.

## Declarations

### CRediT authorship contribution statement

Liangcai Wang: Data curation, Writing-original draft.

Xin Feng, Jielong Wu, Yu Chen: Writing-Reviewing and Editing.

**Huanhuan Ma, Jianbin Zhou:** Supervision, Writing-Review, editing, and funding acquisition.

### Notes

The authors declare no competing financial interest.

## ACKNOWLEDGMENT

This work was supported by the National Promotion Project of China (No. 2020133136), the National Key Research and Development Plan of China (2016YFE0201800).

## References

1. Melikoglu, M. Pumped hydroelectric energy storage: analysing global development and assessing potential applications in Turkey based on vision 2023 hydroelectricity wind and solar energy targets. *Renew Sust Energ Rev* **2017**, 72:146-153. DOI:10.1016/j.rser.2017.01.060.
2. Taira, S., Kurihara, M., Koda, K., et al. TEMPO-oxidized cellulose nanofiber-reinforced lignin based polyester films as a separator for electric double-layer capacitor. *Cellulose* **2019**, 26(1):569-580. DOI:10.1007/s10570-018-2101-z.
3. Jung, M, J., Jeong, E., Lim, J. W., et al. Physico-chemical surface modification of activated carbon by oxyfluorination and its electrochemical characterization. *Colloid Surface A* **2011**, 389(1-3):274-280. DOI:10.1016/j.colsurfa.2011.08.013.
4. Huang, P., Lethien, C., Pinaud, S., et al. On-chip and freestanding elastic carbon films for micro-supercapacitors. *Science* **2016**, 351(6274):691-695. DOI:10.1126/science.aad3345.
5. Sevilla, M., Mokaya, R. Energy storage applications of activated carbons: Supercapacitors and hydrogen storage. *Energ Environ Sci* **2014**, 7(4):1250-1280. DOI:10.1039/c3ee43525c.
6. Ma, X. J., Ding, C. F., Li, D. N., et al. A facile approach to prepare biomass-derived activated carbon hollow fibers from wood waste as high-performance supercapacitor electrodes. *Cellulose* **2018**, 25:4743-4755. DOI:10.1007/s10570-018-1903-3.
7. Li, C., Zhang, X., Wang, K., et al. Scalable self-propagating high-temperature synthesis of graphene for supercapacitors with superior power density and cyclic stability. *Adv Mater* **2016**, 29(7):1604690. DOI:10.1002/adma.201604690.
8. Peng, L., Liang, Y. R., Dong, H. W., et al. Super-hierarchical porous carbons derived from mixed biomass wastes by a stepwise removal strategy for high-performance supercapacitors. *J Power Sources* **2018**, 377:151-160. DOI:10.1016/j.jpowsour.2017.12.012.
9. Qiu, Z. P., Wang, Y. S., Xu, B., et al. Biochar-based carbons with hierarchical micro-meso-macro porosity for high rate and long cycle life supercapacitors. *J Power Sources* **2018**, 376:82-90. DOI:10.1016/j.jpowsour.2017.11.077.
10. Wei, T. Y., Wei, X. L., Yang, L. W., et al. A one-step moderate-explosion assisted carbonization strategy to sulfur and nitrogen dual-doped porous carbon nanosheets derived from camellia petals for energy storage. *J Power Sources* **2016**, 331:373-381. DOI:10.1016/j.jpowsour.2016.09.053.
11. Gong, Y. N., Li, D. L., Luo, C. Z., et al. Highly porous graphitic biomass carbon as advanced electrode materials for supercapacitors. *Green Chem* **2017**, 19(17):4132-4140. DOI:10.1039/c7gc01681f.
12. Wang, C. J., Wu, D. P., Wang, H. J., et al. A green and scalable route to yield porous carbon sheets from biomass for supercapacitors with high capacity. *J Mater Chem A* **2018**, 6(3):1244-1254.

DOI:10.1039/C7TA07579K.

13. Hou, J. H., Jiang, K., Wei, R., et al. Popcorn-derived porous carbon flakes with an ultrahigh specific surface area for superior performance supercapacitors. *Acs Appl Mater Inter* **2017**, 9(36):30626-30634. DOI:10.1021/acsami.7b07746.
14. Chen, X., Chi, M. Z., Xing, L. L., et al. Natural plant template-derived cellular framework porous carbon as a high-rate and long-life electrode material for energy storage. *Acs Sustain Chem Eng* **2019**, 7(6):5845-5855. DOI:10.1021/acssuschemeng.8b05777.
15. Zhang, H., Chen, T., Li, Y., et al. Novel lignin-containing high-performance adhesive for extreme environment. *Int J Biol Macromol* **2020**, 16(1):1832-1839. DOI:10.1016/j.ijbiomac.2020.07.307
16. Passoth, V., Sandgren, M. Biofuel production from straw hydrolysates: current achievements and perspectives. *Appl Microbiol Biot* **2019**, 103(13):5105-5116. DOI:10.1007/s00253-019-09863-3.
17. Xin, J. N., Zhang, P., Wolcott, M. P., et al. A novel and formaldehyde-free preparation method for lignin amine and its enhancement for soy protein adhesive. *J Environ Polym Degr* **2017**, 25(3):599-605. DOI:10.1007/s10924-016-0844-x.
18. Ma, Z. M., Li, S. L., Qiao, W., et al. Hydrothermal degradation of enzymatic hydrolysis lignin in water-isopropyl alcohol co-solvent. *Bioresources* **2016**, 11(3):6867-6879. DOI:10.15376/biores.11.3.6867-6879.
19. Yan, L. C., Cui, Y. H., Gou, G. J., et al. Liquefaction of lignin in hot-compressed water to phenolic feedstock for the synthesis of phenol-formaldehyde resins. *Compos B-Eng* **2016**, 112:8-14. DOI:10.1016/j.compositesb.2016.10.094.
20. Zhu, J. H., Zhang Q, Chen, H. P., et al. Setaria viridis-inspired electrode with polyaniline decorated on porous heteroatom-doped carbon nanofibers for flexible supercapacitors. *Acs Appl Mater Inter* **2020**, 12(39):43634-43645. DOI:10.1021/acsami.0c10933.
21. Zhang, Q., Han, K. H., Li, S. J., et al. Synthesis of garlic skin-derived 3D hierarchical porous carbon for high-performance supercapacitors. *Nanoscale*, **2018**, 10(5):2427-2437. DOI:10.1039/c7nr07158b.
22. Su, H., Zhang, H. T., Liu, F. Y., et al. High power supercapacitors based on hierarchically porous sheet-like nanocarbons with ionic liquid electrolytes. *Chem Eng J* **2017**, 322:73-81. DOI:10.1016/j.cej.2017.04.012.
23. Shang, T. X., Xu, Y., Li, P., et al. A bio-derived sheet-like porous carbon with thin-layer pore walls for ultrahigh-power supercapacitors. *Nano Energy* **2020**, 70:104531. DOI:10.1016/j.nanoen.2020.104531.
24. Díez, N., Ferrero, G. A., Sevilla, M., et al. A sustainable approach to hierarchically porous carbons from tannic acid and their utilization in supercapacitive energy storage systems. *J Mater Chem A* **2019**, 7(23):14280-14290. DOI:10.1039/C9TA01712G.
25. Luo, Z. J., Lin, N., Sun, M. C., et al. Synthesis of 3D-interconnected hierarchical porous carbon from heavy fraction of bio-oil using crayfish shell as the biological template for high-performance supercapacitors. *Carbon* **2021**, 173:910-917. DOI:10.1016/j.carbon.2020.11.083.

26. Ma, H. H., Zhang, Y. M., Wang, L. C., et al. Kinetic analysis of the pyrolysis of apricot stone and its main components via distributed activation energy mode. *Bioresources* **2020**, 15(1):1187-1204. DOI:10.15376/biores.15.1.1187-1204.
27. Li, C. X., Liang, X. R., Gu, J. Preparation and characterization of bagasse nanocellulose. *Chem Res Chinese U* **2017**, 38(7):1286-1294. DOI:10.7503/cjcu20160831.
28. Ren, X., Meng, J., Chang, J., et al. Effect of blending ratio of loblolly pine wood and bark on the properties of pyrolysis bio-oils. *Fuel Process Technol* **2017**, 167:43-49. DOI: 10.1016/j.fuproc.2017.06.025.
29. Park, J., Riaz, A., Insyani, R., et al. Understanding the relationship between the structure and depolymerization behavior of lignin. *Fuel* **2018**, 217(APR.1):202-210. DOI:10.1016/j.fuel.2017.12.079.
30. Ma, Z. H., Chen, D. Y., Gu, J., et al. Determination of pyrolysis characteristics and kinetics of palm kernel shell using TGA-FTIR and model-free integral methods. *Energ. Convers. Manage.* **2015**, 89, 251-259.
31. Yang, H. P., Yan, R., Chen, H. P., et al. Characteristics of hemicellulose, cellulose and lignin pyrolysis. *Fuel* **2007**, 86, 1781-1788.
32. Montane, D., Torne-Fernandez, V., Fierro, V. Activated carbons from lignin: Kinetic modeling of the pyrolysis of Kraft lignin activated with phosphoric acid. *Chem Eng J* **2005**, 106(1):1-12. DOI:10.1016/j.cej.2004.11.001.
33. Zulkefli, N. N., Masdar, M. S., Wan Isahak, W. N. R., et al. Removal of hydrogen sulfide from a biogas mimic by using impregnated activated carbon adsorbent. *Plos One* **2019**, 14(2):e0211713 - e0211713. DOI: 10.1371/journal.pone.0211713.
34. Zhang, L. X., Gu, H. Z., Sun, H. B., et al. Molecular level one-step activation of agar to activated carbon for high performance supercapacitors. *Carbon* **2018**, 132:573-579. DOI:10.1016/j.carbon.2018.02.100.
35. Barbieri, O., Hahn, M., Herzog, A., et al. Capacitance limits of high surface area activated carbons for double layer capacitors. *Carbon* **2005**, 43(6):1303-1310. DOI:10.1016/j.carbon.2005.01.001.
36. Janes, A., Lust, E. Micro- and mesoporous carbon based electrode materials for electrical double layer capacitors. *ECS Transactions* **2008**, 6(25):269-278. DOI: 10.1149/1.2943247.
37. Nagano, S., Tamon, H., Adzumi, T., et al. Activated carbon from municipal waste. *Carbon* **2000**, 38(6):915-920. DOI:10.1016/S0008-6223(99)00208-0.
38. Yang, M. H., Kim, D. S., Hong, S. B., et al. MnO<sub>2</sub> nanowire/biomass-derived carbon from hemp stem for high-performance supercapacitors. *Langmuir* **2017**, 33(21):5140-5147. DOI:10.1021/acs.langmuir.7b00589.
39. Zhang, Y. Y., Gao, Z., Song, N. N., et al. High-performance supercapacitors and batteries derived from activated banana-peel with porous structures. *Electrochim Acta* **2016**, 222:1257-1266. DOI:10.1016/j.electacta.2016.11.099.

40. Sudhan, N., Subramani, K., Karnan, M., et al. Biomass-derived activated porous carbon from rice straw for a high-energy symmetric supercapacitor in aqueous and non-aqueous electrolytes. *Energy Fuel* **2017**, 31(1):977-985. DOI:10.1021/acs.energyfuels.6b01829.
41. Zhang, L. J., Or, W. S. Self-assembled three-dimensional macroscopic graphene/mxene-based hydrogel as electrode for supercapacitor. *APL Mater* **2020**, 8(9):091101. DOI:10.1063/5.0015426.
42. Wang, J. G., Liu, H. Z., Sun, H. H., et al. One-pot synthesis of nitrogen-doped ordered mesoporous carbon spheres for high-rate and long-cycle life supercapacitors. *Carbon* **2018**, 127:85-92. DOI:10.1016/j.carbon.2017.10.084.
43. Chen, L. F., Zhang, X. D., Liang, H. W., et al. Synthesis of nitrogen-doped porous carbon nanofibers as an efficient electrode material for supercapacitors. *Acs Nano* **2012**, 6(8):7092-7102. DOI:10.1016/j.carbon.2017.10.084
44. Zhu, J. H., Zhang, Q., Chen, H. P., et al. Setaria viridis-inspired electrode with polyaniline decorated on porous heteroatom-doped carbon nanofibers for flexible supercapacitors. *Acs Appl Mater Inter* **2020**, 12(39):43643-43645. DOI:10.1021/acsami.0c10933.
45. Zhang, H. F., He, X. J., Wei, F., et al. Moss-covered rock-like hybrid porous carbons with enhanced electrochemical properties. *Acs Sustain Chem Eng* **2020**, 8(8):3065-3071. DOI:10.1021/acssuschemeng.9b05075.
46. Zhao, G. Y., Chen, C., Yu, D. F., et al. One-step production of O-N-S co-doped three-dimensional hierarchical porous carbons for high-performance supercapacitors. *Nano Energy* **2018**, 47:547-555. DOI:10.1016/j.nanoen.2018.03.016.
47. Song, S. J., Ma, F. W., Wu, G., et al. Facile self-template large scale preparation of biomass-derived 3D hierarchical porous carbon for advanced supercapacitors. *J Mater Chem A* **2015**, 3(35):18154-18162. DOI:10.1039/C5TA04721H.
48. Zhang, Y., Liu, S. S., Zheng, X. Y., et al. Biomass organs control the porosity of their pyrolyzed carbon. *Adv Funct Mater* **2016**, 27(3):1604687. DOI:10.1002/adfm.201604687.
49. Zhang, H. T., Zhang, L., Chen, J., et al. One-step synthesis of hierarchically porous carbons for high-performance electric double layer supercapacitors. *J Power Sources* **2016**, 315:120-126. DOI:10.1016/j.jpowsour.2016.03.005.
50. Nanaji, K., Upadhyayula, V., Rao, T. N., et al. Robust, environmentally benign synthesis of nanoporous graphene sheets from bio-waste for ultrafast supercapacitor application. *Acs Sustain Chem Eng* **2018**, 7(2):2516-2529. DOI:10.1021/acssuschemeng.8b05419.
51. Ki, S. J., Lee, H., Park, Y. K., et al. Assessing the electrochemical performance of a supercapacitor electrode made of copper oxide and activated carbon using liquid phase plasma. *Appl Surf Sci* **2018**, 446:243-249. DOI:10.1016/j.apsusc.2018.01.044.
52. Gao, M., Fu, J. W., Wang, M. H., et al. A self-template and self-activation co-coupling green strategy to synthesize high surface area ternary-doped hollow carbon microspheres for high performance supercapacitors. *J Colloid Interf Sci* **2018**, 524:165-176. DOI:10.1016/j.jcis.2018.04.027.

53. Liu, Y., Li, L., Zhu, J. X., et al. A biomimetic *Setaria viridis*-inspired electrode with polyaniline nanowire arrays aligned on MoO<sub>3</sub>@polypyrrole core-shell nanobelts. *J Mater Chem A* **2018**, 6 (27):13428-13437. DOI:10.1039/C8TA04218G.
54. Wang, Y. H., Dong, L. Y., Lai, G. P., et al. Nitrogen-doped hierarchically porous carbons derived from polybenzoxazine for enhanced supercapacitor performance. *Nanomaterials-basel* **2019**, 9(1):131. DOI:10.3390/nano9010131.
55. Borchardt, L., Leistenschneider, D., Haase, J., et al. Revising the concept of pore hierarchy for ionic transport in carbon materials for supercapacitors. *Adv Energy Mater* **2018**, 8(24):1800892. DOI:10.1002/aenm.201800892.
56. Siwińska-Ciesielczyk, K., Kurc, B., Rymarowicz, D., et al. Crystallization of TiO<sub>2</sub>-MoS<sub>2</sub> hybrid material under hydrothermal treatment and its electrochemical performance. *Materials* **2020**, 13(12):2706. DOI:10.3390/ma13122706.
57. Yang, C., Denno, M. E., Pyakurel, P., et al. Recent trends in carbon nanomaterial-based electrochemical sensors for biomolecules: A review. *Anal Chim Acta* **2015**, 887:17-37. DOI:10.1016/j.aca.2015.05.049.
58. Deng, J. Q., Chen, L., Hong, S., et al. UZnCl<sub>2</sub>-DES assisted synthesis of phenolic resin-based carbon aerogels for capacitors. *J Porous Mat* **2020**, 27(3):789-800. DOI:10.1007/s10934-020-00861-9.

## Tables

**Table 1.** Yield, ultimate, and proximate analysis of apricot shell, apricot shell cellulose, and ASLC.

Samples	Yield (%)	Proximate analysis (wt %, db)			Ultimate analysis (wt %, db)				
		Volatile	Fixed Carbon	Ash	C	H	N	S	O
Apricot shell	100	74.19	17.47	0.64	50.66	5.45	0.12	0.08	43.05
Apricot shell cellulose	24.59	85.02	14.50	0.27	39.62	2.80	0.03	0.03	52.27
ASLC	30.42	82.35	16.92	0.73	54.31	2.43	0.24	0.04	42.98

**Table 2.** Textural properties of AAC.

Samples	Specific surface area (m <sup>2</sup> /g)	Specific pore volume (cm <sup>3</sup> /g)			V <sub>micro</sub> /V <sub>meso</sub> <sup>[9]</sup>	D <sub>ave</sub> (nm)	Pore-wall thickness (nm)
		V <sub>t</sub>	V <sub>micro</sub>	V <sub>meso</sub>			
AAC-P-3	1475.16	1.209	0.376	0.609	61.74	3.27	6.163
AAC-P-4	1370.35	1.271	0.326	0.718	45.40	3.70	6.634
AAC-K-1	1669.94	0.970	0.556	0.248	224.19	2.36	5.444
AAC-K-2	2136.56	1.106	0.698	0.186	375.27	2.07	4.255

**Table 3.** Specific capacitances of AAC.

Work electrodes	0.50 A/g (F/g)	0.75 A/g (F/g)	1.00 A/g (F/g)	1.50 A/g (F/g)	2.00 A/g (F/g)	5.00 A/g (F/g)	10.00 A/g (F/g)	Capacitance retention rate (%) at 10.00 A/g
AAC-P-3	169.14	161.47	154.48	149.39	142.22	125.07	113.98	67.39
AAC-P-4	159.98	155.09	149.69	145.33	139.77	124.48	110.03	68.78
AAC-K-1	188.50	183.08	177.80	174.75	170.20	159.00	150.00	79.58
AAC-K-2	236.00	228.83	222.40	217.65	211.40	196.50	181.00	76.69

## Figures

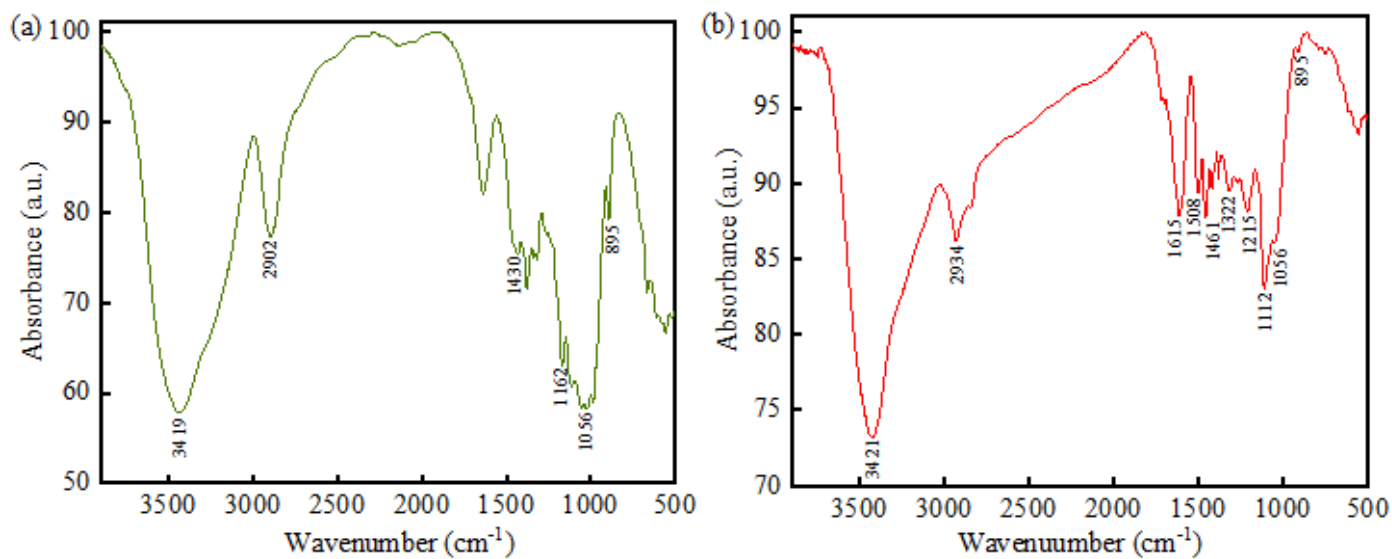


Figure 1

FTIR spectra of apricot shell cellulose (a) and ASLC (b).

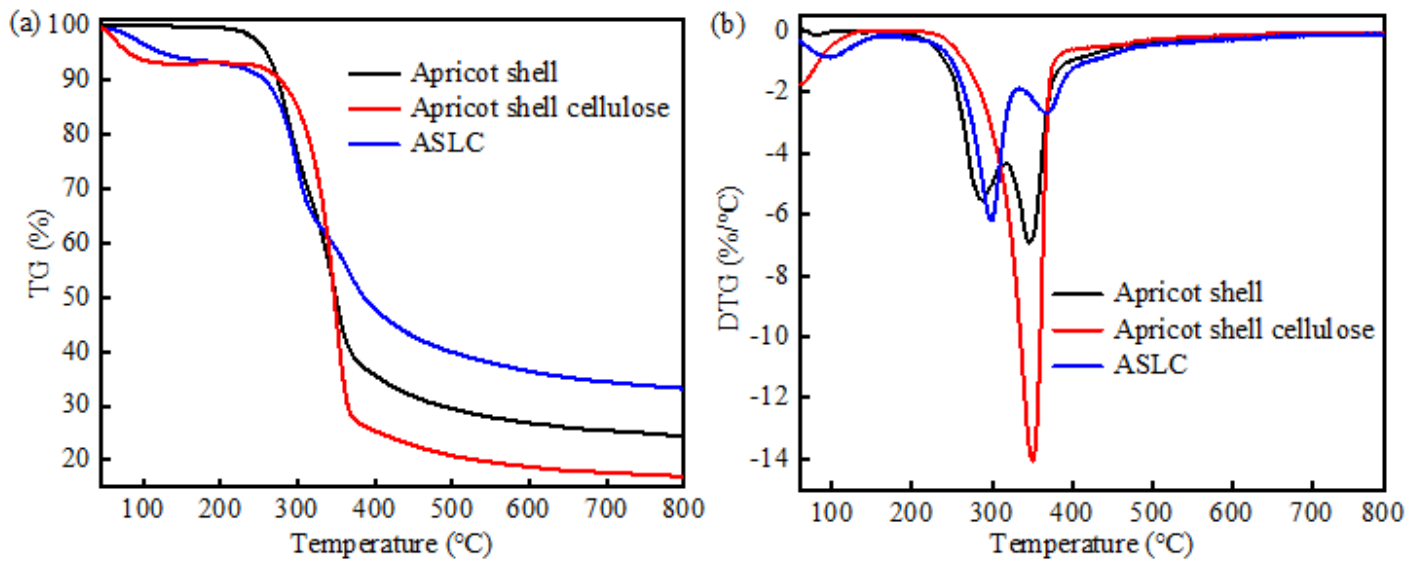


Figure 2

TG (a) and DTG (b) curves of apricot shell, apricot shell cellulose, and ASLC.

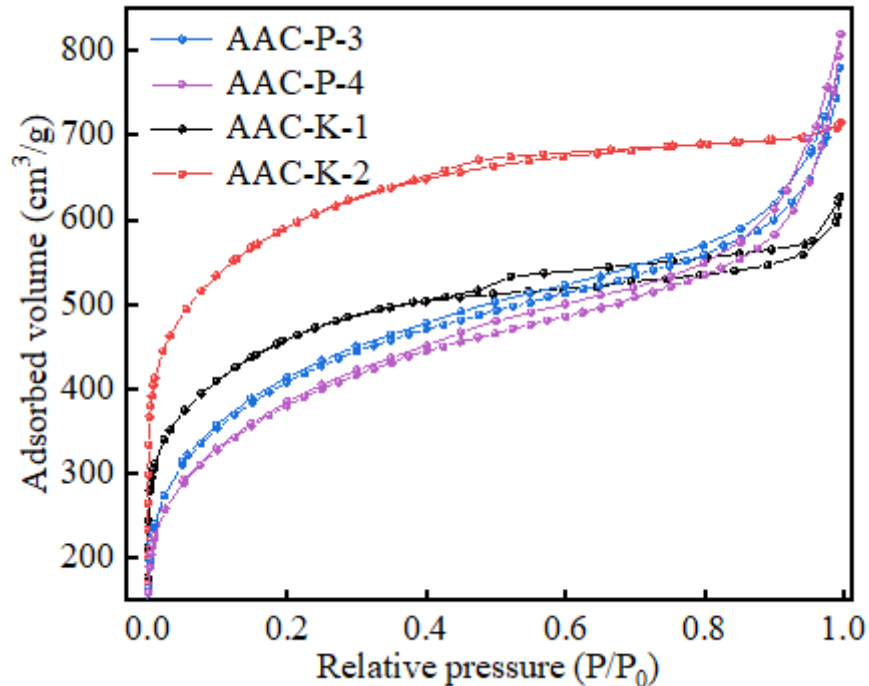


Figure 3

N<sub>2</sub> adsorption/desorption curves.

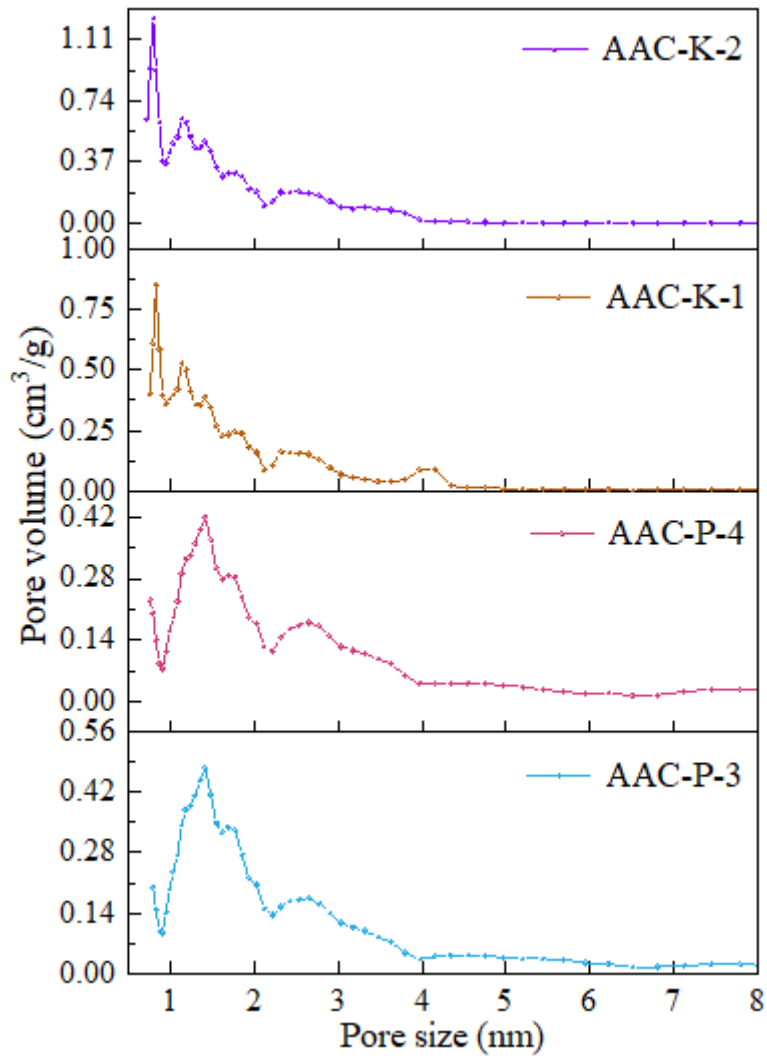


Figure 4

Pore size distribution.

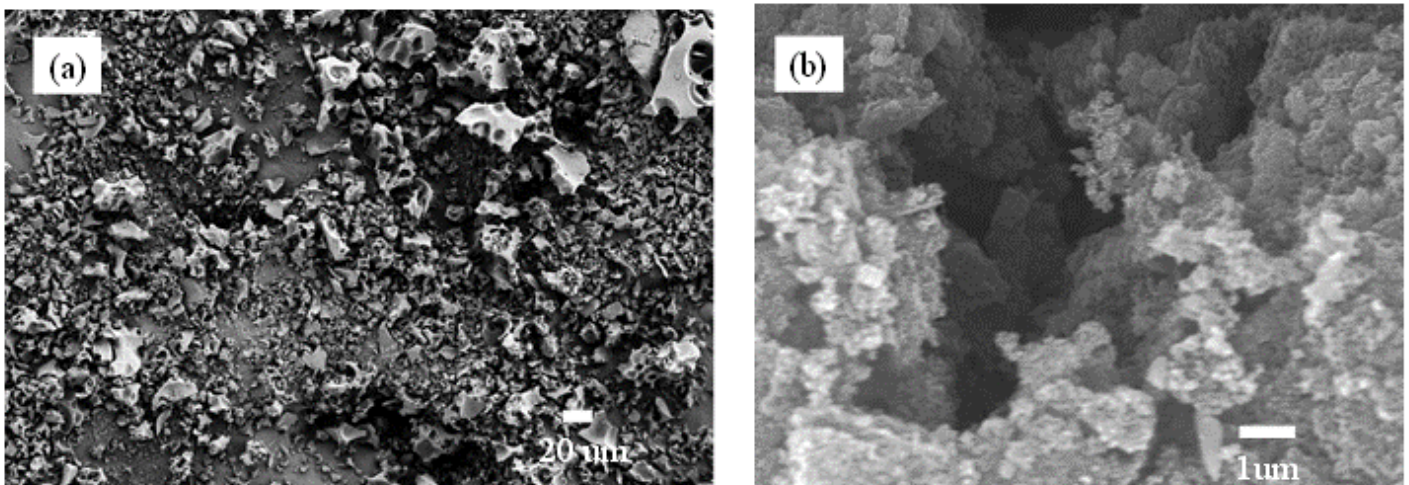
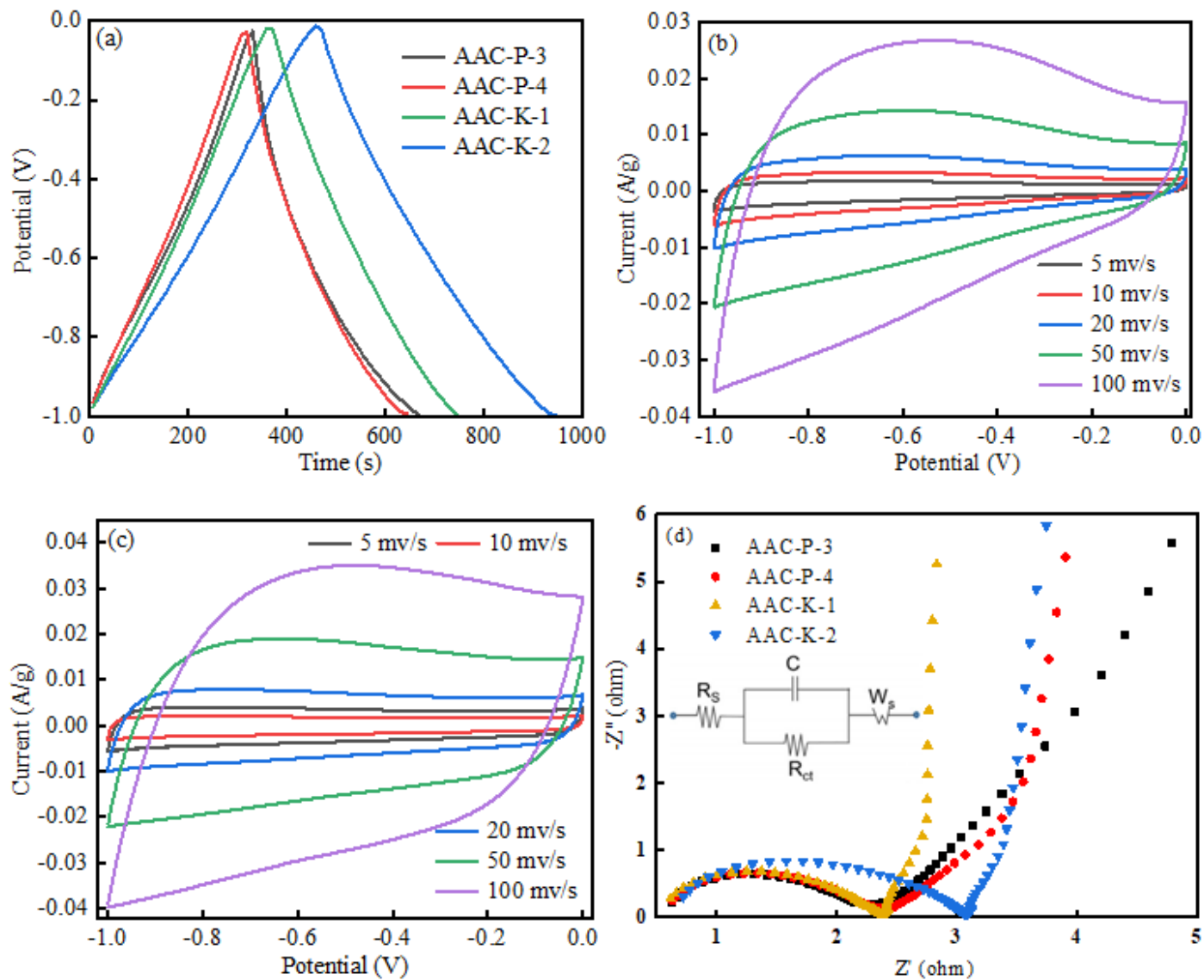


Figure 5

SEM images of AAC-P-3 (a) and AAC-K-2 (b).



**Figure 6**

GCD curves of AAC at 0.5 A/g (a); CV curves of AAC-P-3 (b); CV curves of AAC-K-2 (c); Nyquist plots of AAC in the frequency ranging from 100 kHz to 0.01Hz (d).

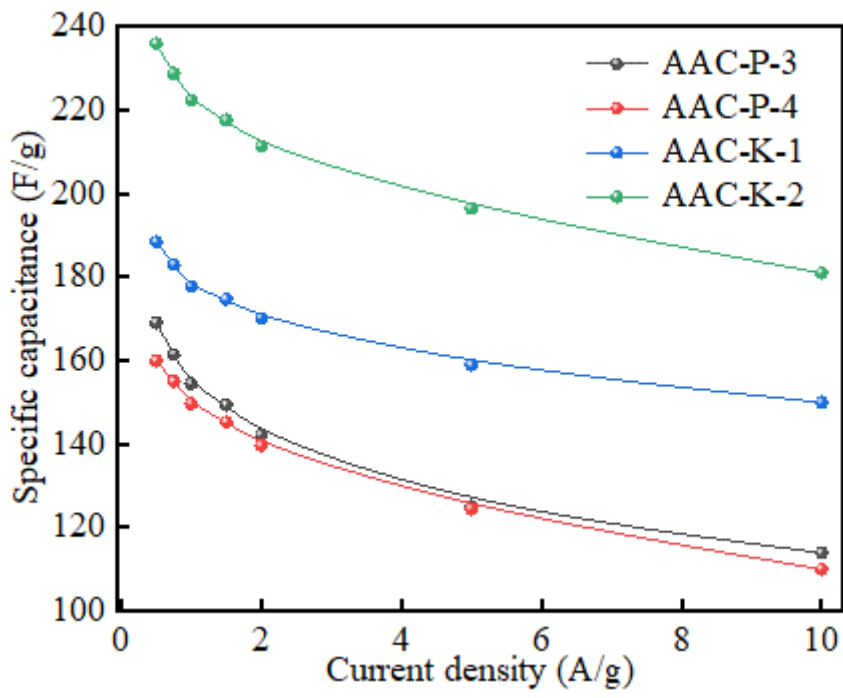
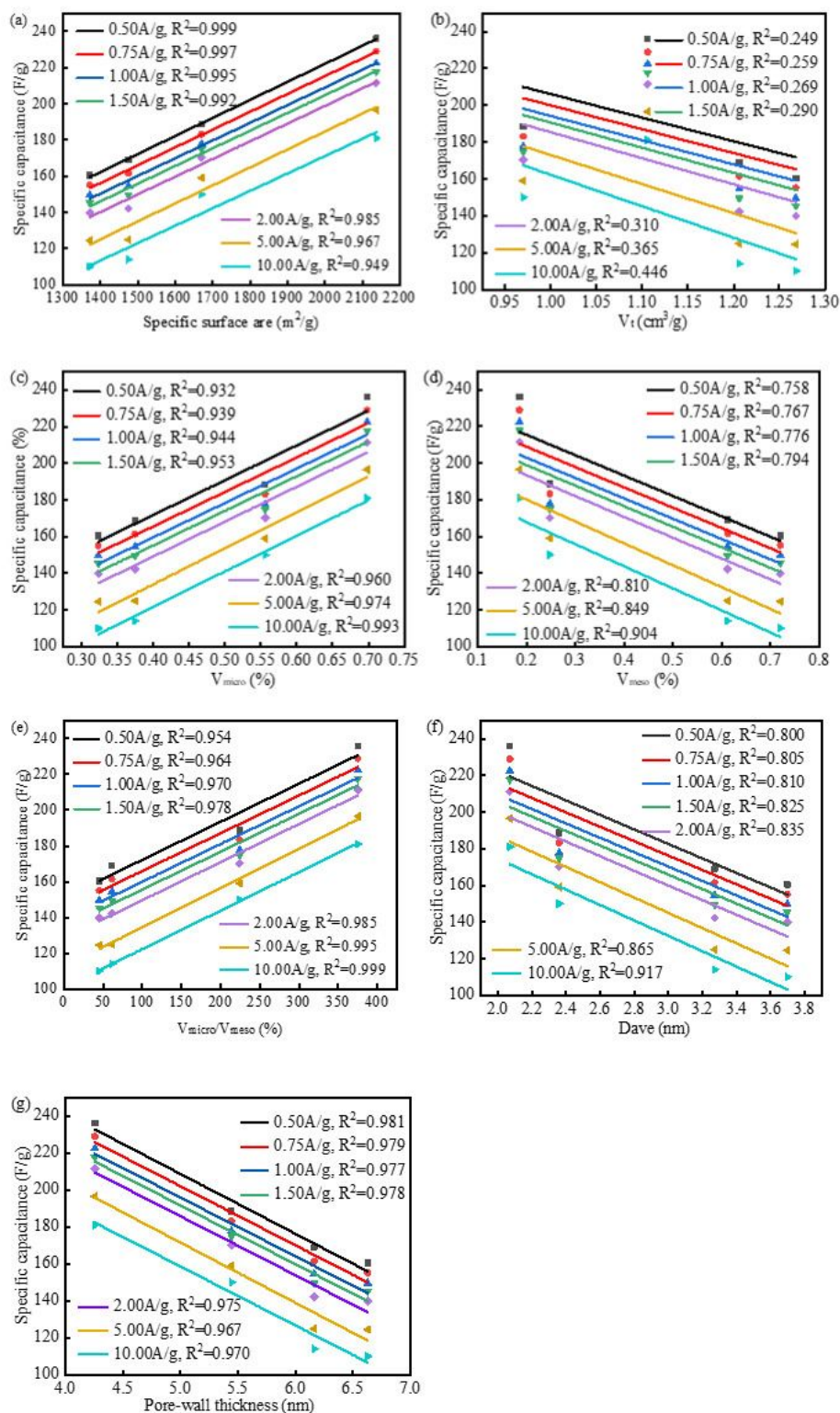


Figure 7

Plot of specific capacitance variation of AAC.



**Figure 8**

The correlation between the textural properties of AAC and its specific capacitance. (a) Specific surface area/specific capacitance correlation. (b) V<sub>t</sub>/specific capacitance correlation. (c) V<sub>micro</sub>/specific capacitance correlation. (d) V<sub>meso</sub>/specific capacitance correlation. (e) V<sub>micro</sub>/V<sub>meso</sub>/specific capacitance correlation. (f) D<sub>ave</sub>/specific capacitance correlation. (g) Pore-wall thickness/specific capacitance correlation.

## Supplementary Files

This is a list of supplementary files associated with this preprint. Click to download.

- [GraphicalAbstractofManuscript.doc](#)